

Titanic magnetoresistance and signature of non-degenerate Dirac nodes in ZrSiS

R. Singha, A. Pariari, B. Satpati, P. Mandal

Saha Institute of Nuclear Physics, 1/AF Bidhannagar, Calcutta 700 064, India

(Dated: December 3, 2024)

We present the results on magnetotransport properties of ZrSiS single crystals. Extremely large, non-saturating magnetoresistance (MR), $\sim 1.4 \times 10^5\%$ at 2 K and 9 T and large anisotropy with different field directions have been observed. The Shubnikov - de Haas oscillation reflects the presence of a small and a large Fermi pocket. Quantum oscillation along with Hall resistance indicate multiple band crossing at different energy levels of electronic band structure with both electron and hole as charge carriers, which is in agreement with the earlier theoretical and ARPES reports. Non-trivial π Berry phase and chiral anomaly confirms the Dirac fermionic nature of the charge carriers.

The search for new topological states of matter is one of the new frontiers in physics. The discovery of topological insulators and subsequent finding of topological Dirac and Weyl semimetals paved the way to study the rich physics involved [1–4]. In Dirac semimetals, the bulk conduction and valence bands cross each other at four-fold degenerate Dirac points protected by time reversal (TRS) and crystal symmetry (CS) [5, 6]. Close to the Dirac points, the bands are linearly dispersing, thus these systems often identified as the three-dimensional analogue of graphene. Shortly after the theoretical prediction [5, 6], the existence of bulk Dirac points have been verified in Cd_3As_2 and Na_3Bi through ARPES and transport measurements [7–10]. While Dirac points are protected by large number of symmetries, by breaking either TRS or inversion symmetry (IS) each Dirac point can be broken into a pair of doubly degenerate Weyl points accompanied by the surface Fermi arc connecting them [5, 6]. The IS breaking compounds TaAs, NbAs, NbP, TaP [11–16] and TRS breaking YbMnBi_2 [17] have been confirmed to host Weyl fermions. Apart from these compounds, a new type of semimetals, namely the topological nodal line semimetals (TNLSM) have emerged, where the band crossings have been observed along one-dimensional closed lines in \mathbf{k} -space instead of discrete points. Although proposed in few materials [18–21], the existence of nodal lines has been experimentally verified only in IS breaking non-centrosymmetric superconducting compound PbTaSe_2 [22, 23], where the nodal rings are protected by reflection symmetry under spin-orbit coupling.

Recently, ARPES measurement and first principle calculations have revealed the existence of multiple Dirac crossings along with an unconventional surface and bulk state hybridization in ZrSiS [24, 25]. The Dirac nodes are protected by non-symmorphic symmetry and reside at different energy values of band structure. The diamond shaped Fermi surface consistent with the band structure calculations has been observed in ARPES measurement. Another feature which, in particular, makes ZrSiS an interesting system is the energy range of the linear band dispersion. While most of the materials observed so far have linear band dispersion up to few hundred meV from the Dirac point, in ZrSiS the range is seen to be as high as 2 eV in some regions of the Brillouin zone.

Here we report the magnetotransport properties of single crystalline ZrSiS. An extremely large, anisotropic magnetoresistance accompanied by Shubnikov-de Haas (SdH) oscillation have been observed and analyzed to calculate the Fermi surface properties of the material.

Single crystals of ZrSiS were grown via iodine vapor transport in two steps. At first, the polycrystalline powder was synthesized using elemental Zr (Alfa Aesar 99.9%), Si (Strem Chem. 99.999%), S (Alfa Aesar 99.9995%) in a process described elsewhere [26]. Then the polycrystalline powder together with iodine in a concentration of 5 mg/cm^3 were sealed in a 20 cm long quartz tube under vacuum. The quartz tube was then kept in a gradient furnace for 72 h with the powder at 1100°C , while the cooler end at 1000°C . Shiny rectangular plate like crystals were obtained at the cooler end for transport measurements.

In Fig.1(a), a typical single crystal of ZrSiS is shown with different crystallographic axis, on which measurements have been done. The crystals cleave perpendicular to \mathbf{c} axis similar to earlier report [25]. High resolution transmission electron microscopy (HRTEM) image of the crystal along \mathbf{ac} plane [Fig.1(b)] confirms the high quality crystalline nature. The electron diffraction patterns obtained in HRTEM measurement are shown in Fig.1(c) and 1(d). The stoichiometry of the grown crystals was verified using energy dispersive X - ray spectroscopy [27]. The transport measurements were performed in a 9 T Physical Property Measurement System (Quantum Design) in \mathbf{ac} transport option by four probe technique.

As shown in Fig.2(a), the zero field resistivity measurement shows the metallic character of ZrSiS. $\rho(T)$ decreases monotonically from 300 K to about 60 K, below which it exhibits a very weak temperature dependence. The resistivity at 2 K becomes as low as $\sim 52 \text{ n}\Omega \text{ cm}$ which is comparable with that of Cd_3As_2 [9]. The residual resistivity ratio $\rho(300 \text{ K})/\rho(2 \text{ K})$ is found to be 288, which is quite large and confirms good metallicity and high quality of the crystals. The resistivity data, in the temperature range 2 to 115 K, can be fitted well with the expression $\rho(T) = A + BT^n$ with $n \sim 3$, shown in Fig.S10 [27]. However $\rho(T)$ is linear in the high temperature region above 115 K. With the application of magnetic field, the low temperature resistivity undergoes

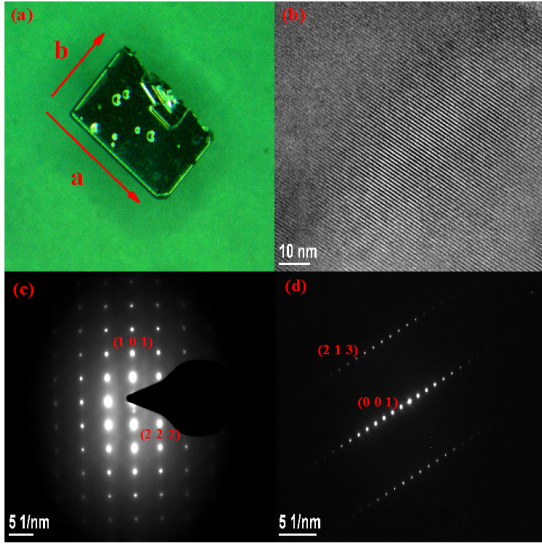


FIG. 1. (a) ZrSiS single crystal with crystal directions. (b) HRTEM image of the crystal. (c) and (d) Selective area electron diffraction (SAED) pattern obtained through HRTEM measurement.

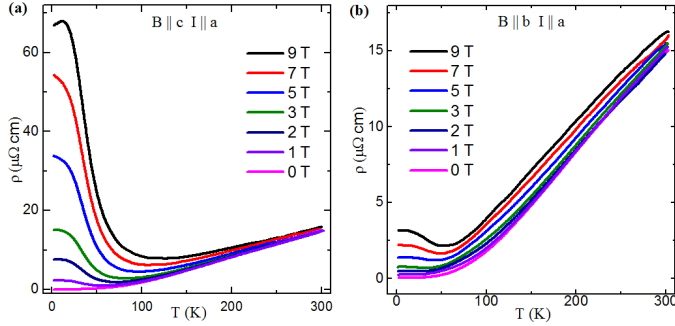


FIG. 2. Temperature dependence of resistivity measured under different transverse magnetic fields when (a) $B \parallel c$ axis, (b) $B \parallel b$ axis.

a drastic enhancement, thus the nature of the slope of $\rho(T)$ curve changes. As a result, a metal-semiconducting like crossover occurs even at a field of 1 T only. This type of magnetic field induced transition, which is often described as a result of gap opening at the band touching points, has already been demonstrated in NbP, WTe₂ and NbSb₂ [14, 28, 29]. It is evident from Fig.2(b) that the metal-semiconducting transition is extremely sensitive to the direction of applied field. With current along **a** axis and magnetic field parallel to **c** axis, a strong crossover has been seen. On the other hand, rotating the field direction by 90°, i.e. parallel to **b** axis, results in much weaker metal - semiconductor like crossover, which occurs at higher field strength. This implies an anisotropic electrical transport with magnetic field applied along two different crystallographic axis.

In both the cases, the transition temperature (T_m) increases monotonically with increasing field showing

$T_m \propto (B - B_0)^{1/\nu}$ type relation (Fig.S11) [27]. ν has a value ~ 3 for both applied field directions, deviating from a value 2 for compensated semimetal Bi, WTe₂ and graphite [30, 31]. Considering the thermal activated transport as in the case of intrinsic semiconductor [32, 33], $\rho(T) = \rho_0 \exp(E_g/2k_B T)$, we have calculated the values of the thermal activation energy gaps 23.44 meV and 3.56 meV at 9 T, for field directions along **c** axis and **b** axis, respectively. The calculated gap E_g shows a magnetic field dependence [27].

The transverse magnetoresistance (MR), i.e. the change in resistance with magnetic field (up to 9 T) applied perpendicular to the current direction has been measured at several temperatures from 2 to 300 K, where MR is defined as, $[(\rho(B) - \rho(0))/\rho(0)] \times 100 \%$. As shown in Fig.3(a) at some representative temperatures, with current parallel to **a** axis and magnetic field along **c** axis, an extremely large, non saturating MR is obtained at low temperatures. At 2 K with a magnetic field 9 T, MR is $1.4 \times 10^5 \%$ which is comparable to that of the Dirac semimetal Cd₃As₂ (MR = $1.6 \times 10^5 \%$ at 2.5 K, 15 T) [9] and the Weyl semimetal candidates such as TaAs (MR = $8 \times 10^4 \%$ at 1.8 K, 9 T) [13], NbP (MR = $8.5 \times 10^5 \%$ at 1.85 K, 9 T) [14], NbAs (MR = $2.3 \times 10^5 \%$ at 2 K, 9 T) [16], WTe₂ (MR = $4.5 \times 10^5 \%$ at 4.5 K, 14.7 T) [28] and NbSb₂ (MR = $1.3 \times 10^5 \%$ at 2 K, 9 T) [29]. With the increase in temperature, MR decreases dramatically with a value of just about 14 % at 300 K in 9 T. At low fields, MR shows a quadratic field dependence ($\propto B^2$), which with increasing field becomes almost linear. As shown in Fig. S14 [27], the MR data at different temperatures can not be rescaled to a single curve using Kohler's rule $MR = \alpha(\mu_0 H/\rho_0)^m$. The violation of Kohler rule suggests the presence of more than one type of carrier and/or the different temperature dependence of their mobilities [31, 34].

It is apparent from the resistivity data that the transverse MR is highly anisotropic in nature. Applying field parallel to **b** axis and keeping the current direction unchanged, the MR has been seen to reduce to $\sim 7000 \%$ at 5 K and 9 T. The MR has a value of 12 % at 300 K and 9 T. At 3 K with a magnetic field 9 T, the anisotropic ratio $\rho(B \parallel c)/\rho(B \parallel b)$ has a large value 21 which is comparable to that reported in NbSb₂ (20 at 2 K, 9 T) [29].

Next, to measure the longitudinal MR (LMR), both the current and magnetic fields are applied along **a** axis. As shown in Fig.3(c), negative MR has been observed at 2 K and low fields. With the increase in temperature, however, the negative MR progressively weakens and then vanishes. This negative MR has been ascribed to induce Adler-Bell-Jackiw chiral anomaly in Dirac system in time reversal symmetry broken realization under application of magnetic field [6]. Chiral anomaly is caused by the chiral charge imbalance in the system resulting in a net flow of fermions between two Weyl nodes of opposite chirality. The chiral magnetic effect, a long sought phenomena proposed in relativistic quantum field theory, has been

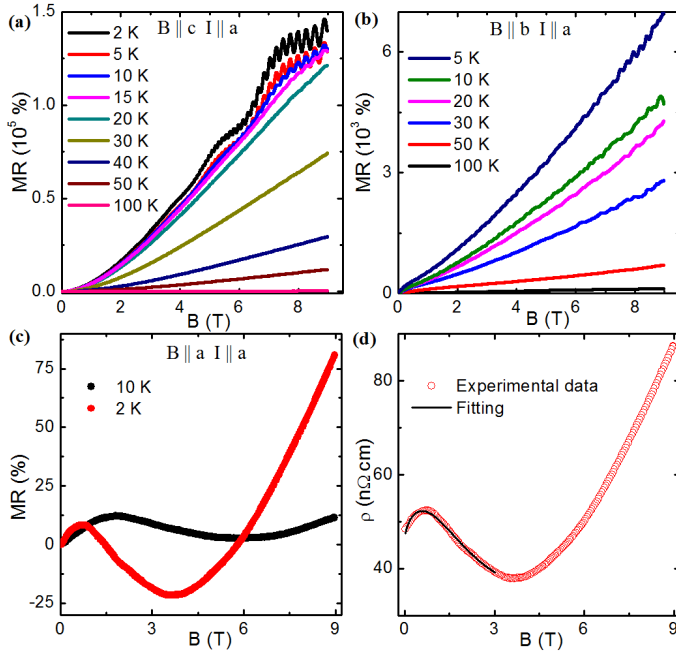


FIG. 3. Transverse magnetoresistance with current along **a** axis and magnetic field parallel to (a) **c** axis and (b) **b** axis, measured at different temperatures, up to 9 T. (c) Longitudinal magnetoresistance (LMR) with current and field along **a** axis. (d) Fitting of LMR data at 2 K using semiclassical formula.

demonstrated through negative MR in Dirac semimetals Cd_3As_2 [35], Na_3Bi [36], ZrTe_5 [37] and Weyl semimetal TaAs [13], under parallel electric and magnetic field. MR becomes positive at higher fields, which may be due to small misalignment of **E** and **B**. The negative MR can be analyzed using the semiclassical formula [13]

$$\sigma(B) = (1 + C_w H^2) \cdot (\sigma_0 + a\sqrt{H}) + (\rho_0 + AH^2)^{-1} \quad (1)$$

where σ_0 is the zero field conductivity and C_w is a parameter originating from topological **E** · **B**. Fig.3(d) illustrates the good agreement between the fitting and experimental data.

Another interesting feature which emerges from the transport measurement is the presence of SdH oscillation traceable at fields even below 2 T and temperature up to 20 K. This not only gives an insight into the nature of the Fermi surface, but also it is an evidence of very high mobility of the charge carriers present in the system. From the oscillatory data, it is clear that there are more than one frequency present. To extract the oscillatory component $\Delta\rho(B)$, a smooth background is subtracted from the field dependent resistivity $\rho(B)$. To deconvolute the two components of oscillation, the background subtraction has been done in two steps.

In Fig.4(a) and Fig.4(b), $\Delta\rho(B)$ for two different components is plotted as a function of $1/B$ at some representative temperatures. The fast Fourier transform (FFT) analysis of the components reveals oscillation frequencies

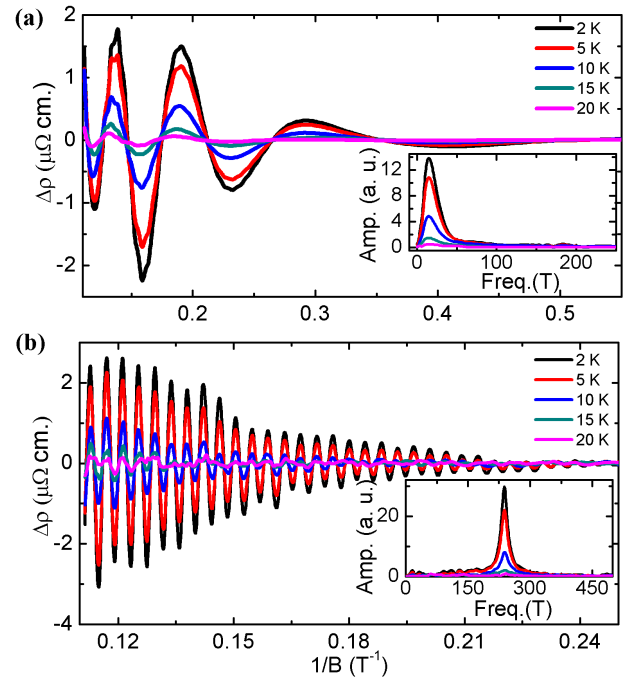


FIG. 4. SdH oscillation obtained by subtracting smooth background from magnetoresistance measurement, plotted with inverse magnetic field ($1/B$) at different temperatures for two deconvoluted components. The insets in both figures show the corresponding FFT results.

14.15 T and 238.24 T, respectively. The obtained frequencies indicate the existence of a very large and a small Fermi surface cross-sections perpendicular to **c** axis. Using the Onsager relationship

$$F = (\varphi_0/2\pi^2)A_F \quad (2)$$

where φ_0 is the single magnetic flux quantum and A_F is the Fermi surface cross-section perpendicular to the applied magnetic field, we have calculated cross-sections $1.35 \times 10^{-3} \text{ \AA}^{-2}$ and $22.7 \times 10^{-3} \text{ \AA}^{-2}$ for 14.15 T and 238.24 T frequencies, respectively. Considering circular geometry of the cross-section, we obtain Fermi momentum $2.07 \times 10^{-2} \text{ \AA}^{-1}$ and $8.5 \times 10^{-2} \text{ \AA}^{-1}$, respectively for smaller and larger Fermi pockets.

In Fig.5(a), the oscillation amplitude is shown as a function of temperature. To determine the cyclotron effective mass (m^*) of the charge carriers, we have fitted the oscillation amplitude for both frequencies using thermal damping factor in Lifshitz - Kosevich formula,

$$R_T = (2\pi^2 k_B T / \beta) / \sinh(2\pi^2 k_B T / \beta) \quad (3)$$

where $\beta = e\hbar B/m^*$. The cyclotron effective masses of the charge carriers are determined to be $\sim 0.14 m_0$ and $\sim 0.1 m_0$ for 238.24 T and 14.15 T frequencies, respectively. m_0 is the rest mass of the free electron. The corresponding Fermi velocities ($v_F = \hbar k_F/m^*$), $6.93 \times 10^5 \text{ m/s}$ and $2.37 \times 10^5 \text{ m/s}$ have been calculated, which are quite large.

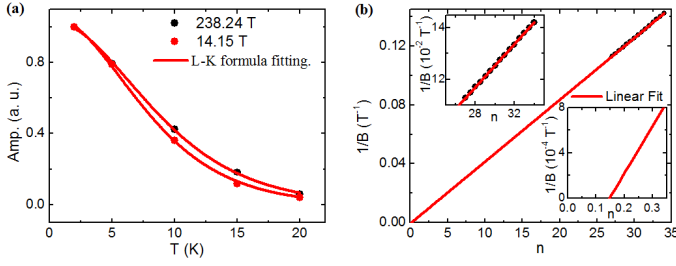


FIG. 5. (a) Temperature dependence of relative amplitude of SdH oscillation for both Fermi pockets. (b) Landau level index plot for 238.24 T frequency oscillation. Upper and lower inset shows the experimental data points and the intercept by extrapolated linear fitting, respectively.

To get the carrier density, we have employed the relation with the oscillation frequency [38, 39]

$$\Delta \left(\frac{1}{B} \right) = \frac{2e}{\hbar} \left(\frac{g_s g_v}{6\pi^2 n_{3D}} \right)^{2/3} \quad (4)$$

where g_s and g_v are the spin and valley degeneracies. We have calculated carrier densities $2.07 \times 10^{19} / \text{cm}^3$ and $3 \times 10^{17} / \text{cm}^3$ for larger and smaller frequencies respectively. From the magnetic field induced damping of oscillation amplitude, $\Delta\rho \propto \exp(-2\pi^2 k_B m^* T_D / \hbar e B)$, Dingle temperatures (T_D) are determined to be 11.18 K and 3.4 K for two oscillation components at 2 K. To get an quantitative estimate about the mobility of the charge carriers in the system, we have calculated the quantum mobility $\mu_q = (e\hbar/2\pi k_B m^* T_D)$. The obtained values, $\sim 1.35 \times 10^3 \text{ cm}^2 \text{ V}^{-1} \text{ s}^{-1}$ and $\sim 6.2 \times 10^3 \text{ cm}^2 \text{ V}^{-1} \text{ s}^{-1}$ for larger and smaller frequencies respectively, show the significant difference between the mobilities of the carriers associated with two different Fermi pockets. The value of the quantum mobility in a system is always lower than the value of the classical Drude mobility (μ_c), as μ_q is sensitive to both large and small angle scattering, while μ_c is sensitive to only large angle scattering [40]. Therefore, the carrier mobility in ZrSiS are expected to be higher than the calculated values from quantum oscillation. This is also evident from the very low residual resistivity at low temperatures.

With magnetic field along **b** axis, no clear oscillation has been recorded within 9 T applied field. This may be due to heavier effective mass and low mobility of the charge carriers along that direction.

To determine the nature of the charge carriers, as shown in Fig.5(b), Landau level fan diagram for the larger Fermi pocket has been plotted, assigning maxima of the SdH oscillation as integers and minima as half integers. Extrapolated linear fitting gives an intercept of 0.15 (shown in the inset), which is very close to the range $\pm 1/8$ for Dirac fermions [41]. For 14.15 T Fermi pocket, however, the numbers of maxima and minima positions are quite small within our experimental range of magnetic field. Therefore, we are unable to show the Landau

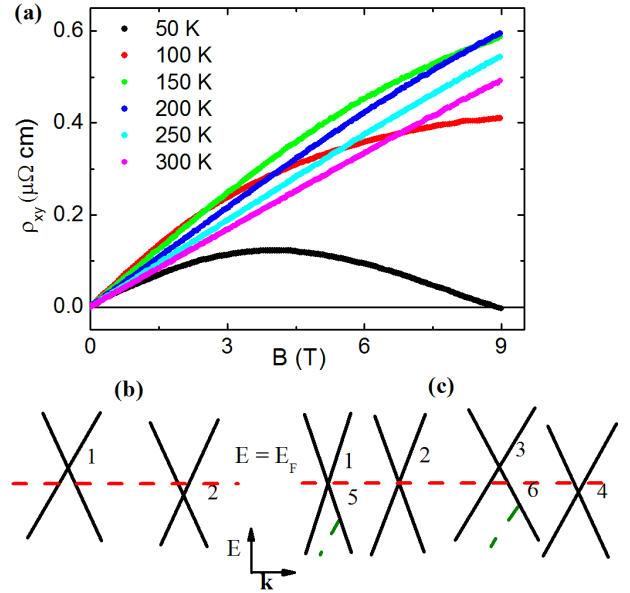


FIG. 6. (a) Field dependence of Hall resistivity measured at different temperatures. (b) Schematic explaining transport measurement results. (c) Schematic illustrating multiple Dirac cones in ZrSiS as described in earlier reports [24, 25].

index plot for the small Fermi pocket.

To determine the sign of the charge carriers from the two Fermi pockets, Hall effect measurement was performed. At 300 K, the Hall resistivity is found out to be almost linear with field and positive, which indicates holes as majority carriers. Earlier report at room temperature, also showed holes as majority carriers [25]. Upon decreasing the temperature, the Hall resistivity develops a sublinear character. Around 50 K, the Hall resistivity changes its sign from positive to negative at high magnetic fields. Thus the existence of more than one type of carriers is confirmed. The overall behavior of the Hall resistivity can be understood by considering low mobility carriers associated with large Fermi pocket as hole type and higher mobility carriers bound to small Fermi pocket as electron type. From the above, it is clear that at least two band crossings are present in the electronic band structure of ZrSiS at different energy values, as shown schematically in Fig. 6(b).

The earlier report of ARPES and band structure calculations suggest the presence of multiple Dirac crossings at different energy values as illustrated in the schematic Fig. 6(c). As shown, the Dirac cones 3 and 4 cross the Fermi energy, having Dirac points at two different energy values. Among others, 1 and 2 have their band crossing points almost at the chemical potential energy with negligible Fermi surface volume, while 5 and 6 are lying at much lower energies. Thus in this configuration, it is expected that only signature of Dirac cones 3 and 4 will be observed in the transport properties of ZrSiS, which is consistent with our magneto-transport results.

In summary, we report the magneto-electronic trans-

port properties of ZrSiS single crystals. Magnetic field induced metal-semiconductor crossover along with a strong anisotropic MR have been observed. Transverse MR approaches an extremely large value $\sim 1.4 \times 10^5$ % at 2 K and 9 T, without any sign of saturation. Under parallel \mathbf{E} and \mathbf{B} , the observed negative MR confirms Adler-Bell-Jackiw chiral anomaly in ZrSiS. The SdH oscillation reveals two inequivalent Fermi surface cross-sections perpendicular to crystallographic \mathbf{c} axis. Fermi velocity, Fermi momentum and cyclotron effective mass have

been calculated from the oscillation in transport properties. The presence of Dirac fermions is confirmed from the calculated non-trivial π Berry phase. Non-linear field dependence of Hall resistivity indicates the presence of both electron and hole type of carriers. SdH oscillation along with Hall measurement reflect multiple band crossings at different energy values of the band structure.

Acknowledgement: We thank N. Khan, A. Paul and S. Roy for their help during measurements and useful discussions.

-
- [1] M. Z. Hasan, C. L. Kane, *Rev. Mod. Phys.* **82**, 3045 (2010).
 - [2] X. L. Qi, S. C. Zhang, *Rev. Mod. Phys.* **83**, 1057 (2011).
 - [3] H. Zhang, C.-X. Liu, X.-L. Qi, X. Dai, Z. Fang, S.-C. Zhang, *Nat. Phys.* **5**, 438 (2009).
 - [4] Y. L. Chen, J. G. Analytis, J.-H. Chu, Z. K. Liu, S.-K. Mo, X. L. Qi, H. J. Zhang, D. H. Lu, X. Dai, Z. Fang, S. C. Zhang, I. R. Fisher, Z. Hussain, Z.-X. Shen, *Science* **325**, 178 (2009).
 - [5] Z. Wang, Y. Sun, X.-Q. Chen, C. Franchini, G. Xu, H. Weng, X. Dai, Z. Fang, *Phys. Rev. B* **85**, 195320 (2012).
 - [6] Z. Wang, H. Weng, Q. Wu, X. Dai, Z. Fang, *Phys. Rev. B* **88**, 125427 (2013).
 - [7] Z. K. Liu, J. Jiang, B. Zhou, Z. J. Wang, Y. Zhang, H. M. Weng, D. Prabhakaran, S.-K. Mo, H. Peng, P. Dudin, T. Kim, M. Hoesch, Z. Fang, X. Dai, Z. X. Shen, D. L. Feng, Z. Hussain, Y. L. Chen, *Nat. Mat.* **13**, 677 (2014).
 - [8] M. Neupane, S. Y. Xu, R. Sankar, N. Alidoust, G. Bian, C. Liu, I. Belopolski, T. R. Chang, H. T. Jeng, H. Lin, A. Bansil, F. Chou, M. Z. Hasan, *Nat. Commun.* **5**, 3786 (2014).
 - [9] T. Liang, Q. Gibson, M. N. Ali, M. Liu, R. J. Cava, N. P. Ong, *Nat. Mat.* **14**, 280 (2015).
 - [10] Z. K. Liu, B. Zhou, Y. Zhang, Z. J. Wang, H. M. Weng, D. Prabhakaran, S. K. Mo, Z. X. Shen, Z. Fang, X. Dai, Z. Hussain, Y. L. Chen, *Science* **343**, 864 (2014).
 - [11] H. Weng, C. Fang, Z. Fang, B. A. Bernevig, X. Dai, *Phys. Rev. X* **5**, 011029 (2015).
 - [12] S.-Y. Xu, I. Belopolski, N. Alidoust, M. Neupane, C. Zhang, R. Sankar, S. - M. Huang, C.- C. Lee, G. Chang, B. Wang, G. Bian, H. Zheng, D. S. Sanchez, F. Chou, H. Lin, S. Jia, M. Z. Hasan, *Science* **349**, 613 (2015).
 - [13] X. Huang, L. Zhao, Y. Long, P. Wang, D. Chen, Z. Yang, H. Liang, M. Xue, H. Weng, Z. Fang, X. Dai, G. Chen, *Phys. Rev. X* **5**, 031023 (2015).
 - [14] C. Shekhar, A. K. Nayak, Y. Sun, M. Schmidt, M. Nicklas, I. Leermakers, U. Zeitler, Y. Skourski, J. Wosnitza, Z. Liu, Y. Chen, W. Schnelle, H. Borrmann, Y. Grin, C. Felser, B. Yan, *Nat. Phys.* **11**, 645 (2015).
 - [15] J. Hu, J.Y. Liu, D. Graf, S.M.A Radmanesh, D.J. Adams, A. Chuang, Y. Wang, I. Chiorescu, J. Wei, L. Spinu, Z. Q. Mao, *Scien. Reports* **6**, 18674 (2016).
 - [16] N. J. Ghimire, Y. Luo, M. Neupane, D. J. Williams, E. D. Bauer, F. Ronning, *J. Phys. Cond. Matt.* **27**, 152201 (2015).
 - [17] S. Borisenko, D. Evtushinsky, Q. Gibson, A. Yaresko, T. Kim, M. N. Ali, B. Buechner, M. Hoesch, R. J. Cava, *arXiv:1507.04847* (2015).
 - [18] Y. Kim, B. J. Wieder, C. L. Kane, A. M. Rappe, *Phys. Rev. Lett.* **115**, 036806 (2015).
 - [19] R. Yu, H. Weng, Z. Fang, X. Dai, X. Hu, *Phys. Rev. Lett.* **115**, 036807 (2015).
 - [20] L. S. Xie, L. M. Schoop, E. M. Seibel, Q. D. Gibson, W. Xie, R. J. Cava, *Appl. Phys. Lett. Mater.* **3**, 083602 (2015).
 - [21] G. Bian, T.-R. Chang, H. Zheng, S. Velury, S.-Y. Xu, T. Neupert, C.-K. Chiu, S.-M. Huang, D. S. Sanchez, I. Belopolski, N. Alidoust, P.-J. Chen, G. Chang, A. Bansil, H.-T. Jeng, H. Lin, M. Z. Hasan, *arXiv:1508.07521* (2015).
 - [22] G. Bian, T.-R. Chang, R. Sankar, S.-Y. Xu, H. Zheng, T. Neupert, C.-K. Chiu, S.-M. Huang, G. Chang, I. Belopolski, D. S. Sanchez, M. Neupane, N. Alidoust, C. Liu, B. K. Wang, C.-C. Lee, H.-T. Jeng, C. Zhang, Z. Yuan, S. Jia, A. Bansil, F. Chou, H. Lin, M. Z. Hasan, *Nat. Commun.* **7**, 10556 (2016).
 - [23] M. N. Ali, Q. D. Gibson, T. Klimczuk, R. J. Cava, *Phys. Rev. B* **89**, 020505(R) (2014).
 - [24] Q. Xu, Z. Song, S. Nie, H. Weng, Z. Fang, X. Dai, *Phys. Rev. B* **92**, 205310 (2015).
 - [25] L. M. Schoop, M. N. Ali, C. Straßer, V. Duppel, S. S. P. Parkin, B. V. Lotsch, C. R. Ast, *arXiv:1509.00861* (2015).
 - [26] A. K. Haneveld, F. Jellinek, *Recueil des Travaux Chimiques des Pays-Bas* **83**, 776 (1964).
 - [27] See supplementary information for 'Titanic magnetoresistance and signature of non-degenerate Dirac nodes in ZrSiS.' [Url will be provided by the publisher.]
 - [28] M. N. Ali, J. Xiong, S. Flynn, J. Tao, Q. D. Gibson, L. M. Schoop, T. Liang, N. Haldolaarachchige, M. Hirschberger, N. P. Ong, R. J. Cava, *Nature* **514**, 205 (2014).
 - [29] K. Wang, D. Graf, L. Li, L. Wang, C. Petrovic, *Scien. Reports* **4**, 7328 (2014).
 - [30] Y. Kopelevich, J. C. Medina Pantoja, R. R. da Silva, S. Moehlecke, *Phys. Rev. B* **73**, 165128 (2006).
 - [31] Y. L. Wang, L. R. Thoutam, Z. L. Xiao, J. Hu, S. Das, Z. Q. Mao, J. Wei, R. Divan, A. Luican-Mayer, G. W. Crabtree, W. K. Kwok, *Phys. Rev. B* **92**, 180402(R) (2015).
 - [32] J. Hu, T. F. Rosenbaum, *Nat. Mat.* **7**, 697 (2008).
 - [33] T. Hirahara, Y. Sakamoto, Y. Saisyu, H. Miyazaki, S. Kimura, T. Okuda, I. Matsuda, S. Murakami, S. Hasegawa, *Phys. Rev. B* **81**, 165422 (2010).
 - [34] R. H. McKenzie, J. S. Qualls, S. Y. Han, J. S. Brooks, *Phys. Rev. B* **57**, 11854 (1998).
 - [35] H. Li, H. He, H.-Z. Lu, H. Zhang, H. Liu, R. Ma, Z. Fan,

- S.-Q. Shen, J. Wang, Nat. Commun. **7**, 10301 (2016).
- [36] J. Xiong, S. K. Kushwaha, T. Liang, J. W. Krizan, M. Hirschberger, W. Wang, R. J. Cava, N. P. Ong, Science **350**, 413 (2015).
- [37] Q. Li, D. E. Kharzeev, C. Zhang, Y. Huang, I. Pletikoscic, A. V. Fedorov, R. D. Zhong, J. A. Schneeloch, G. D. Gu, T. Valla, Nat. Phys. **3648** (2016).
- [38] D. Shoenberg, Magnetic oscillations in metals, Cambridge Univ. Press, (1984).
- [39] J. Feng, Y. Pang, D. Wu, Z. Wang, H. Weng, J. Li, X. Dai, Z. Fang, Y. Shi, L. Lu, Phys. Rev B **92**, 081306(R) (2015).
- [40] A. Narayanan, M. D. Watson, S. F. Blake, N. Bruyant, L. Drigo, Y. L. Chen, D. Prabhakaran, B. Yan, C. Felser, T. Kong, P. C. Canfield, A. I. Coldea, Phys. Rev. Lett. **114**, 117201 (2015).
- [41] H. Murakawa, M. S. Bahramy, M. Tokunaga, Y. Kohama, C. Bell, Y. Kaneko, N. Nagaosa, H. Y. Hwang, Y. Tokura, Science **342**, 1490, (2013).

Supplementary information: Titanic magnetoresistance and signature of non-degenerate Dirac nodes in ZrSiS

For crystal structure determination, electron diffraction of ZrSiS single crystal has been done along different zone axis, using high resolution transmission electron microscopy (HRTEM) in FEI, TECNAI G² F30, S - TWIN microscope operating at 300 kV equipped with a GATAN Orius SC1000B CCD camera. From the diffraction data, interplanar spacing and subsequently the Miller indices of the lattice planes have been extracted.

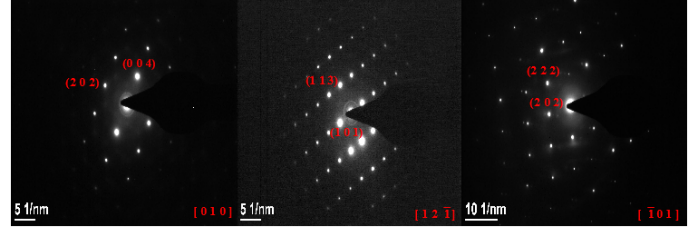


Fig.S 7. Electron diffraction images of ZrSiS crystals with corresponding zone axis, obtained through HRTEM measurements.

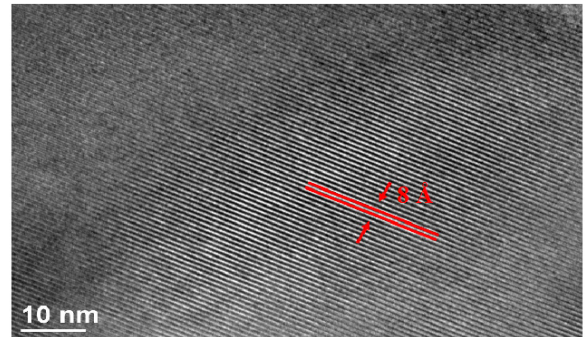


Fig.S 8. HRTEM image along **ac** - plane.

To check the stoichiometry, we have performed Energy - dispersive X - ray (EDX) spectroscopy of the grown ZrSiS crystals using same microscope with scanning unit and high - angle annular dark - field scanning (HAADF) detector from Fischione (Model 3000). The obtained spectrum is shown in Fig.S9. The result of elemental analysis is in very good agreement with the initial molar ratio of the starting elements.

The zero field resistivity shows two regions with different temperature dependence. As shown in the Fig.S10, at low temperature T^3 dependence is followed by almost linear dependence at high temperature.

Field induced metal-semiconductor crossover is indicated by the increase in resistivity with decreasing temperature. The transition temperature (T_m) is identified as the temperature where resistivity minimum oc-

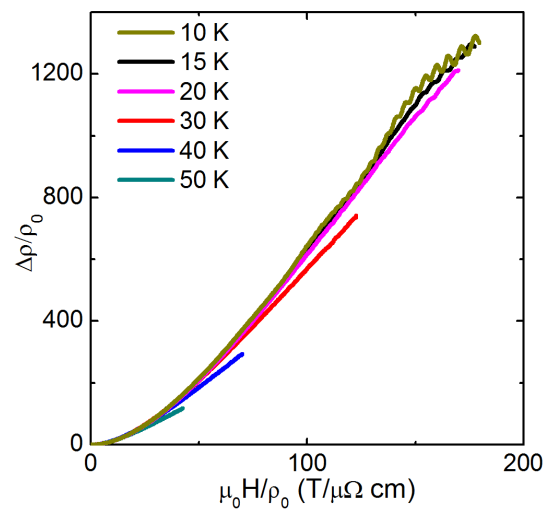


Fig.S 14. The Kohler's rule scaling of MR data with field parallel to **c** axis.